



CHALMERS

Chalmers Publication Library

Linear and nonlinear characterization of low-stress high-confinement silicon-rich nitride waveguides

This document has been downloaded from Chalmers Publication Library (CPL). It is the author's version of a work that was accepted for publication in:

Optics Express (ISSN: 1094-4087)

Citation for the published paper:

Krückel, C. ; Fülöp, A. ; Klintberg, T. et al. (2015) "Linear and nonlinear characterization of low-stress high-confinement silicon-rich nitride waveguides". Optics Express, vol. 23(20), pp. 25827-25837.

Downloaded from: <http://publications.lib.chalmers.se/publication/225822>

Notice: Changes introduced as a result of publishing processes such as copy-editing and formatting may not be reflected in this document. For a definitive version of this work, please refer to the published source. Please note that access to the published version might require a subscription.

Chalmers Publication Library (CPL) offers the possibility of retrieving research publications produced at Chalmers University of Technology. It covers all types of publications: articles, dissertations, licentiate theses, masters theses, conference papers, reports etc. Since 2006 it is the official tool for Chalmers official publication statistics. To ensure that Chalmers research results are disseminated as widely as possible, an Open Access Policy has been adopted. The CPL service is administrated and maintained by Chalmers Library.

(article starts on next page)

Linear and nonlinear characterization of low-stress high-confinement silicon-rich nitride waveguides

Clemens J. Krüchel,* Attila Fülöp, Thomas Klintberg,
Jörgen Bengtsson, Peter A. Andrekson, and Víctor Torres-Company

*Photonics Laboratory, Department of Microtechnology and Nanoscience, Chalmers
University of Technology, SE-412 96 Gothenburg, Sweden*

*kruckel@chalmers.se

Abstract: In this paper we introduce a low-stress silicon enriched nitride platform that has potential for nonlinear and highly integrated optics. The manufacturing process of this platform is CMOS compatible and the increased silicon content allows tensile stress reduction and crack free layer growth of 700 nm. Additional benefits of the silicon enriched nitride is a measured nonlinear Kerr coefficient n_2 of $1.4 \cdot 10^{-18}$ m²/W (5 times higher than stoichiometric silicon nitride) and a refractive index of 2.1 at 1550 nm that enables high optical field confinement allowing high intensity nonlinear optics and light guidance even with small bending radii. We analyze the waveguide loss (~ 1 dB/cm) in a spectrally resolved fashion and include scattering loss simulations based on waveguide surface roughness measurements. Detailed simulations show the possibility for fine dispersion and nonlinear engineering. In nonlinear experiments we present continuous-wave wavelength conversion and demonstrate that the material does not show nonlinear absorption effects. Finally, we demonstrate microfabrication of resonators with high Q -factors ($\sim 10^5$).

© 2015 Optical Society of America

OCIS codes: (130.3120) Integrated optics devices; (130.7405) Wavelength conversion devices; (160.6000) Semiconductor materials; (190.4380) Nonlinear optics, four-wave mixing; (220.4241) Nanostructure fabrication; (230.5750) Resonators.

References and links

1. M. J. R. Heck, J. F. Bauters, M. L. Davenport, D. T. Spencer, and J. E. Bowers, "Ultra-low loss waveguide platform and its integration with silicon photonics," *Laser Photon. Rev.* **8**(5), 667–686 (2014).
2. W. D. Sacher, Y. Huang, G. -Q. Lo, and J. K. S. Poon, "Multilayer silicon nitride-on-silicon integrated photonic platforms and devices," *J. Lightwave Technol.* **33**(4), 901–910 (2015).
3. M. Piels, J. F. Bauters, M. L. Davenport, M. J. R. Heck, and J. E. Bowers, "Low-loss silicon nitride AWG demultiplexer heterogeneously integrated with hybrid III-V/Silicon photodetectors," *J. Lightwave Technol.* **32**(4), 817–823 (2014).
4. R. Heiderman, M. Hoekman, and E. Schreuder, "TriPleX-based integrated optical ring resonators for lab-on-a-chip and environmental detection," *IEEE J. Sel. Top. Quantum Electron.* **18**(5), 1583–1596 (2012).
5. M. Boerkamp, T. van Leest, J. Heldens, A. Leinse, M. Hoekman, R. Heiderman, and J. Caro, "On-chip optical trapping and Raman spectroscopy using a TripleX dual-waveguide trap," *Opt. Express* **22**(25), 30528–30537 (2014).
6. J. F. Bauters, M. J. R. Heck, D. D. John, J. S. Barton, C. M. Bruinink, A. Leinse, R. G. Heiderman, D. J. Blumenthal, and J. E. Bowers, "Planar waveguides with less than 0.1 dB/m propagation loss fabricated with wafer bonding," *Opt. Express* **19**(24), 24090–24101 (2011).

7. J. F. Bauters, J. R. Adleman, M. J. R. Heck, and J. E. Bowers, "Design and characterization of arrayed waveguide gratings using ultra-low loss Si₃N₄ waveguides," *Appl. Phys. A* **116**(2), 427–432 (2014).
8. D. T. Spencer, J. F. Bauters, M. J. R. Heck, and J. E. Bowers, "Integrated waveguide coupled Si₃N₄ resonators in the ultrahigh-Q regime," *Optica* **1**(3), 153–157 (2014).
9. M. Chavez-Boggio, D. Bodenmuller, T. Fremberg, R. Haynes, M. M. Roth, R. Eisermann, M. Lisker, L. Zimmermann, and M. Bohm, "Dispersion engineered silicon nitride waveguides by geometrical and refractive-index optimization," *J. Opt. Soc. Am. B* **31**(11), 2846–2857 (2014).
10. D. J. Moss, R. Morandotti, A. L. Gaeta, and M. Lipson, "New CMOS-compatible platforms based on silicon nitride and Hydex for nonlinear optics," *Nature Photon.* **7**(8), 597–607 (2013).
11. R. Halir, Y. Okawachi, J. S. Levy, M. A. Foster, M. Lipson, and A. L. Gaeta, "Ultrabroadband supercontinuum generation in a CMOS-compatible platform," *Opt. Lett.* **37**(10), 1685–1687 (2012).
12. J. S. Levy, A. Gondarenko, M. A. Foster, A. C. Turner-Foster, A. L. Gaeta, and M. Lipson, "CMOS-compatible multiple-wavelength oscillator for on-chip optical interconnects," *Nature Photon.* **4**(1), 37–40 (2010).
13. F. Ferdous, H. X. Miao, D. E. Leaird, K. Srinivasan, J. Wang, L. Chen, L. T. Varghese, and A. M. Weiner, "Spectral line-by-line pulse shaping of on-chip microresonator frequency combs," *Nature Photon.* **5**(12), 770–776 (2011).
14. T. Herr, K. Hartinger, J. Riemensberger, C. Y. Wang, E. Gavartin, R. Holzwarth, M. L. Gorodetsky, and T. J. Kippenberg, "Universal formation dynamics and noise of Kerr-frequency combs in microresonators," *Nature Photon.* **6**(7), 480–487 (2012).
15. A. Gondarenko, J. S. Levy, and M. Lipson, "High confinement micron-scale silicon nitride high Q ring resonator," *Opt. Express* **17**(14), 11366–11370 (2009).
16. J. P. Epping, M. Hoekman, R. Mateman, A. Leinse, R. G. Heideman, A. van Rees, P. J. M. van der Slot, C. J. Lee, and K. -J. Boller, "High confinement, high yield Si₃N₄ waveguides for nonlinear optical applications," *Opt. Express* **23**(2), 642–648 (2015).
17. K. Luke, A. Dutt, C. B. Poitras, and M. Lipson, "Overcoming Si₃N₄ film stress limitations for high quality factor ring resonators," *Opt. Express* **21**(19), 22829–22833 (2013).
18. M. -C. Cheng, C. -P. Chang, W. -S. Huang, and R. -S. Huang, "Ultralow stress silicon rich nitride films for microstructure fabrication," *Sens. Mater.* **11**(6), 349–358 (1999).
19. T. Barwicz, M. A. Popovic, P. T. Rakich, M. R. Watts, H. A. Haus, E. P. Ippen, and H. I. Smith, "Microring-resonator-based add-drop filters in SiN: fabrication and analysis," *Opt. Express* **12**(7), 1437–1442 (2004).
20. H. T. Philipp, K. N. Andersen, W. Svendsen, and H. Ou, "Amorphous silicon rich nitride optical waveguides for high density integrated optics," *Electron. Lett.* **40**(7), 419–421 (2004).
21. C. Krüchel, A. Fülöp, P. Andrekson, and V. Torres-Company, "Continuous-wave nonlinear optics in low-stress silicon-rich nitride waveguides," in *Proceedings of the Conference on Optical Fiber Communications* (2015), paper W1K.4.
22. K. Ikeda, R. E. Saperstein, N. Alic, and Y. Fainman, "Thermal and Kerr nonlinear properties of plasma-deposited silicon nitride/silicon dioxide waveguides," *Opt. Express* **16**(17), 12987–12994 (2008).
23. J. P. R. Lacey and F. P. Payne, "Radiation loss from planar waveguides with random wall imperfections," *IEEE Proceedings J.* **137**(4), 282–288 (1990).
24. M. Dinu, F. Quochi, and H. Garcia, "Third-order nonlinearities in silicon at telecom wavelengths," *Appl. Phys. Lett.* **82**(18), 2954–2956 (2003).
25. A. D. Bristow, N. Rotenberg, and H. M. van Driel, "Two-photon absorption and Kerr coefficients of silicon for 850–2200 nm," *Appl. Phys. Lett.* **90**(19), 191104-3 (2007).
26. G. E. Jellison, Jr. and F. A. Modine, "Parameterization of the optical functions of amorphous materials in the interband region," *Appl. Phys. Lett.* **69**(3), 371–373 (1996).
27. J. P. R. Lacey and F. P. Payne, "Optical Properties, Band Gap, and Surface Roughness of Si₃N₄," *Phys. Stat. Solidi (A)* **39**(2), 411–418 (1977).
28. V. P. Tzolov and M. Fontaine, "Nonlinear self-phase-modulation effects: a vectorial first-order perturbation approach," *Opt. Lett.* **20**(5), 456–458 (1995).
29. A. Boskovic, S. V. Chernikov, and J. R. Taylor, "Direct continuous-wave measurement of n₂ in various types of telecommunication fiber at 1.55 μm," *Opt. Lett.* **21**(24), 1966–1968 (1996).
30. M. -C. Tien, J. F. Bauters, M. J. R. Heck, D. J. Blumenthal, and J. E. Bowers, "Ultra-low loss Si₃N₄ waveguides with low nonlinearity and high power handling capability," *Opt. Express* **18**(23), 23562–23568 (2010).

1. Introduction

Silicon nitride (Si_xN_y) waveguides constitute a very attractive platform for integrated photonics applications. Similar to silicon-on-insulator (SOI) devices, their fabrication process is fully compatible with CMOS fabrication standards, and they render suitable for hybrid integration with other active components, such as modulators, amplifiers and detectors, both with silicon

and III/V materials [1–3]. A key difference with respect to SOI is that the transparency window of Si_xN_y reaches into the visible and ultraviolet regions, which opens up new opportunities for integrated optics in life science applications [4, 5]. Ultra-low propagation losses of ~ 0.1 dB/m in the optical telecommunication window have been reported for thin (40–50 nm), low confinement, Si_xN_y waveguides [6]. This has enabled the fabrication of high-performance passive devices, such as arrayed waveguide gratings [7] and ultra-high Q resonators [8] of relevance in fiber-optics applications.

Thicker waveguides provide higher optical confinement inside the waveguide core. High confinement allows for shorter curvature radii and, as a result, a higher density of photonic integration. In addition, the relatively high index contrast with respect to the silica cladding allows for engineering the dispersion of the waveguide (see e.g. [9]). This is crucial to achieve broadband phase matching in nonlinear optics applications [10]. Indeed, supercontinuum generation [9, 11], parametric frequency comb generation [12–14] and wavelength conversion [12] have been reported in thick Si_xN_y waveguides. In contrast to SOI waveguides, Si_xN_y shows no sign of two-photon absorption in the optical telecommunications band [10], which allows one to leverage the high-power erbium-doped fiber technology.

A challenge with Si_xN_y waveguides is that films thicker than ~ 300 nm suffer large tensile stress and, in consequence, the waveguides tend to crack [15]. However, for a rectangular waveguide geometry, it is necessary to have very thick waveguides in order to get the zero dispersion wavelength in the telecommunications C-band [16]. Recent works address this manufacturability issue in different ways [16, 17]. In [17], mechanical trenches are inscribed in the oxide layer before the waveguide structures are fabricated. The trenches prevent further propagation of mechanical shock waves that initiate near the edge of the wafer. In this way, a crack-free region where devices can be safely fabricated, is cleared at the center of the wafer. With this method, stoichiometric Si_xN_y (i.e. Si_3N_4) waveguides as thick as 900 nm have been fabricated recently. Epping et al. [16] proposed an alternative method that consists of filling inscribed trenches in the oxide layer with silicon nitride. Hence the filled trench becomes the waveguide's core. Using Si_3N_4 , they achieve propagation losses in the order of 0.4 dB/cm for waveguides of similar thickness.

An interesting feature of Si_xN_y films is that the relative content of Si and N can be precisely adjusted during the deposition process. A different composition in the film has a dramatic effect in the stress [18]. In particular, films with lower stress can be deposited by increasing slightly the content of silicon [19], resulting in crack-free, thick (>500 nm) waveguides as reported e.g. in [20]. In this work, we present a detailed analysis of the linear and nonlinear properties of our thick non-stoichiometric Si_xN_y waveguides [21]. Although the propagation losses (~ 1 dB/cm) are above the values reported by others [16, 17], the nonlinear Kerr coefficient is ~ 5 times higher than stoichiometric Si_3N_4 waveguides [22], resulting in notable nonlinear effects even when operating with continuous-wave (CW) lasers. We provide an in-depth study of the dispersion and nonlinear characteristics and detail our fabrication process. We observe no sign of detrimental two-photon absorption effects in the telecommunications C-band. The high mode confinement allows for manufacturing high-quality factor resonators ($Q \sim 10^5$) with a free spectral range in the order of several nanometers, a record-high value for non-stoichiometric Si_xN_y waveguides. In essence, the presented structure combines in a single platform the beneficial features of stoichiometric silicon nitride (absence of two-photon absorption) with those of SOI waveguides (large nonlinear coefficient), making it very promising for integrated nonlinear optics applications.

The remaining of the work is structured as follows. In Section 2 we describe the fabrication process. Section 3 covers the loss characterization and the simulation results of group velocity dispersion, and the nonlinear coefficient are presented in section 4. In Section 5 nonlinear

experiments are presented, and in Section 6 we summarize the performance of our high- Q microresonators.

2. Fabrication

The manufacturing of the silicon-enriched nitride waveguides is compatible with the mature processing platform to fabricate complementary metal-oxide-semiconductor (CMOS) systems, which gives the option for mass production of integrated optics devices. A detailed schematic of the fabrication procedure of our Si_xN_y waveguides is presented in Fig. 1(a). To simplify matters, only the upper part of the wafer processing is shown so that the symmetric layer growth on the backside is not part of the schematic. Starting from a plain silicon wafer (P-doped/Boron, $\langle 100 \rangle$ orientation) in the first step, a 2 μm layer of buried-oxide is grown in a thermal wet oxidation process in H_2O environment. On top of the silicon dioxide film a layer of silicon-enriched nitride is deposited in a low-pressure chemical vapor deposition (LPCVD) process. By varying the gas composition of the film forming reactants NH_3 and SiH_2Cl_2 injected into the reaction chamber, the ratio of the silicon and nitrogen content in the Si_xN_y film can be adjusted. The recipe we used results in a ratio of around 65% silicon to 35% nitrogen that enables a tensile stress reduced growth of Si_xN_y films with a thickness of 700 nm. The film

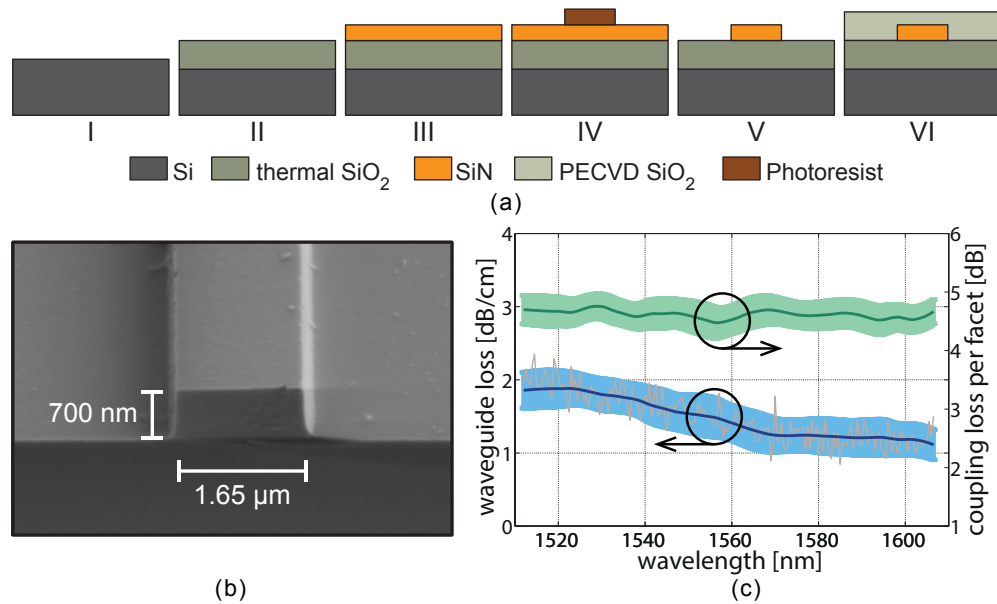


Fig. 1. (a) Schematic of fabrication process for silicon-enriched nitride waveguides. Only the processing of the top part of the wafer is presented. (I) Silicon wafer as initial condition. (II) Thermal wet oxidation of 2 μm SiO_2 . (III) LPCVD deposition of 700 nm silicon-rich nitride in a gas mixture of NH_3 and SiH_2Cl_2 . (IV) Patterning of the photoresist based etching mask by DUV lithography. (V) Dry etching of Si_xN_y in CHF_3 and O_2 and remaining etch mask removal. (VI) PECVD deposition of 2 μm SiO_2 in SiH_4 and N_2O . (b) SEM picture of patterned Si_xN_y strip after etching. Magnification of 70 000. (c) Experimental results of spectrally resolved waveguide loss and coupling loss in Si_xN_y waveguide (700 nm height, 1.65 μm width). The dark lines show the mean value, the bright shadowed areas the standard deviation and the brown curve shows the propagation loss for one sample waveguide, (see details in the text).

composition was measured with energy dispersive X-ray spectroscopy. In order to transfer the transverse waveguide pattern into the Si_xN_y layer we used a photoresist based soft mask during etching which is structured via deep-ultraviolet (DUV) contact lithography. This lithography technique readily enables to resolve feature sizes down to around 200 nm. The smoothness and durability of the etch mask is improved by a descum procedure and a heat treatment at 130 °C for 20 min. In a CHF_3 and O_2 based dry etching step, a Si_xN_y strip is etched with nearly smooth and vertical sidewalls as can be seen in the scanning electron microscope (SEM) picture in Fig. 1(b). The picture reveals that the 700 nm thick silicon-enriched nitride strip is crack free. With our DUV lithography and etching process a 400 nm gap between two waveguides can clearly be resolved as shown in Fig. 2(a). Finally, the 2 μm upper SiO_2 cladding of the waveguide is deposited in a plasma-enhanced vapor deposition (PECVD) step with SiH_4 and N_2O as the reactive gas mixture.

3. Loss characterization

To specify dominant loss contributions in our silicon-enriched nitride waveguides, we combined spectrally resolved transmission scans with the cut-back method. The transmission scans are measured by launching light from a tunable laser into the waveguide and sweeping the wavelength in synchronization with a photodetector to measure the system throughput for individual wavelengths. By calibrating the transmission scans, the fiber-to-fiber loss of the device under test were separated from additional setup loss. The wavelength scans with 189 data points were performed for three different waveguide lengths (1.98, 3.03, 5.01 cm). The transmission loss from three different lengths allows the fitting of a first-order polynomial, to extract propagation loss and coupling loss from the slope and offset of the polynomial. Performing an individual polynomial fit for each wavelength, results in a spectrally resolved characterization of the coupling and propagation loss. In Fig. 1(c) the waveguide propagation loss of one waveguide with 189 wavelength data points is shown. The noise of the curve, resulting from spurious reflection artifacts in the waveguide, was cleaned up using a moving

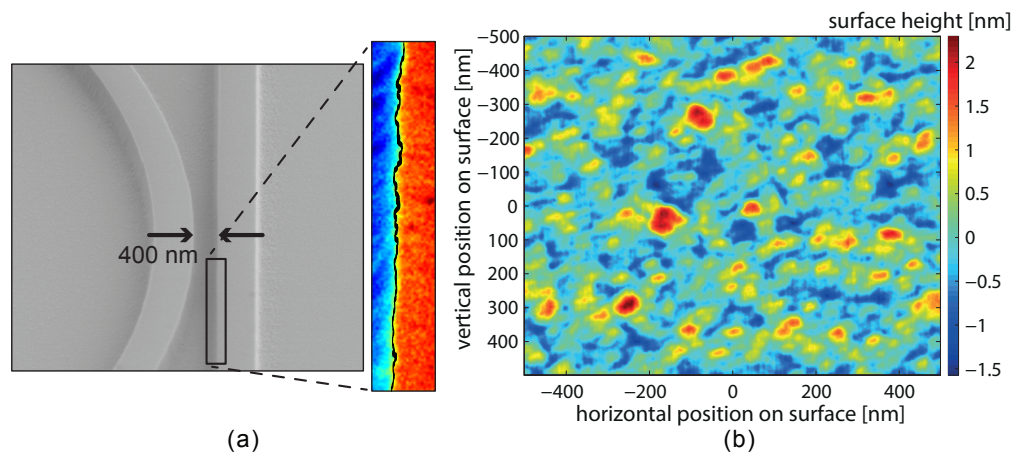


Fig. 2. (a) SEM picture of the coupling region between the bus waveguide and the microring resonator at a magnification of 25 000. The inset shows the indicated rectangular area for the analysis of sidewall roughness, with the SEM image intensity converted to color code. The black line going from top to bottom is the identified edge of the waveguide wall used to extract the roughness parameters. (b) Atomic force microscopy picture of the Si_xN_y surface.

average filter over 20% of the data points. In total, seven different waveguide systems at different locations in the same wafer were evaluated to calculate the mean value and standard deviation for the spectrally resolved propagation and coupling loss as presented in Fig. 1(c). It can be seen that the coupling loss is fairly constant over wavelength with a mean value of around 4.8 dB per facet owing to Fresnel reflections and modal field mismatch between the tapered fiber (spot size 2.5 μm) and the waveguide. The propagation loss decreases from around 1.8 dB/cm at 1510 nm down to 1.2 dB/cm above 1570 nm. This trend indicates dominant material loss over losses from scattering locations in the waveguide boundaries as the higher confinement at shorter wavelength increases the optical wave interaction with the material. The material losses in the C-band could be caused by higher-order vibrational modes of N-H bonds.

We support the claim of dominant material loss at lower wavelength by an estimation of the scattering losses which was done in two steps. First, the surface roughness of the waveguide sidewalls and the top surface was measured for the Si_xN_y waveguide strip after etching. The sidewall roughness was obtained from image processing the top-view SEM pictures of the straight waveguide; a result can be seen as the inset in Fig. 2(a) where the black meandering line indicates the detected position of the sidewall. For the top surface a two-dimensional surface profile was obtained with atomic force microscopy (AFM) and the results are presented in Fig. 2(b). From these measurements we calculated as indicators of the roughness feature size both the root mean square (rms) σ of the roughness height variations and the (auto-)correlation L_c of the fluctuations along the plane of surface. The extracted roughness parameters were $(\sigma, L_c) = (5, 45)$ nm for the sidewall and $(\sigma, L_c) = (0.5, 30)$ nm for the top surface. The bottom surface of the waveguide was not accessible for roughness measurements but it was assumed to have similar roughness parameters as for the top surface. In the second step the parameters were inserted into an expression for the scattering loss originally derived for slab waveguides [23]. It has, however, been widely used also for rectangular waveguides, with some reasonable though not entirely rigorous reinterpretation of the entities in the formula. Since our aim is to qualitatively compare the scattering losses to the total waveguide losses the precision in this approach should be more than sufficient. In addition to the surface roughness parameters, the scattering loss formula also contains some entities for the undisturbed waveguide - without surface roughness - which were obtained from numerical simulations as mentioned in the next section. The loss formula then yielded a total loss from the two sidewalls of ~ 0.2 dB/cm and from the top and bottom interfaces of less than 0.01 dB/cm. The sidewall scattering loss is thus not insignificant but clearly smaller than the absorption loss, judging from the measurements of the total waveguide loss. The strong wavelength dependence of the total loss further underscores that absorption is the dominant loss mechanism, since the scattering loss is virtually independent of the wavelength; the simulations show that increasing the wavelength from 1500 to 1600 nm the sidewall scattering loss decreases by merely 0.01 dB/cm.

4. Simulation of group velocity dispersion and nonlinear coefficient

In order to receive realistic results from mode solver simulations the refractive indices of all three materials forming the waveguide were determined using spectroscopic ellipsometry over the wavelength range from 245 to 1690 nm. The measurements were taken from one point in the middle of the wafer. The measured refractive indices at 1550 nm for the thermally grown and PECVD deposited SiO_2 were around 1.44 and 1.46, and for the silicon-enriched nitride layer it was 2.1. Simulations were then carried out with a finite element method based solver (COMSOL). The high index contrast between core and cladding results in a power distribution mainly confined in the core as presented in Fig. 3(a), here presented for the fundamental

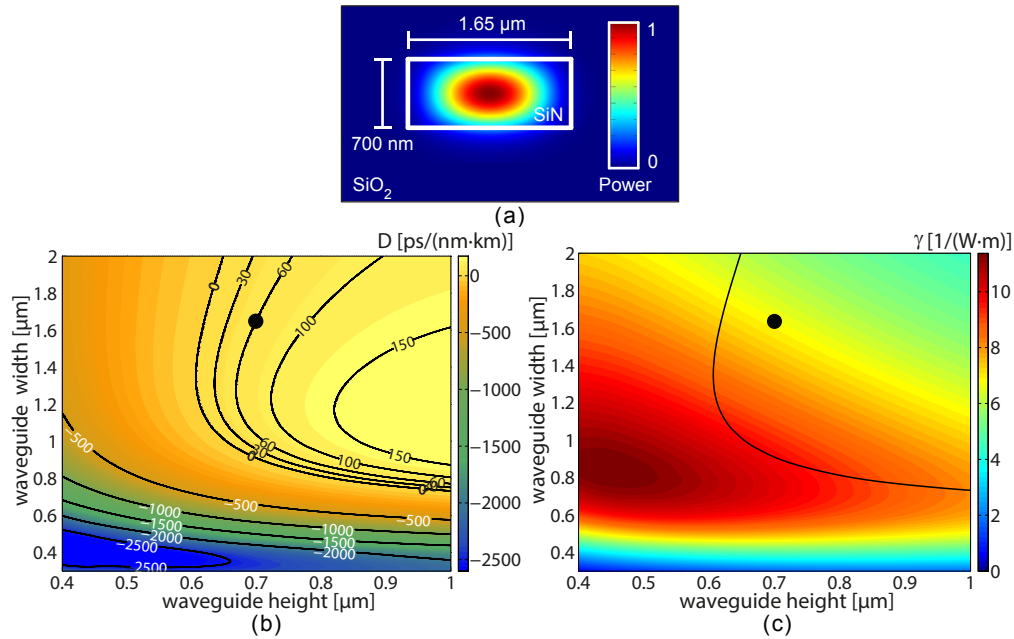


Fig. 3. (a) Simulation of power distribution of the fundamental TE-mode at 1550 nm wavelength. (b) Simulation of dispersion D as a function of waveguide height and waveguide width of the fundamental TE-mode at 1550 nm wavelength. The dot indicates the waveguide dimensions used in this publication. (c) Simulation of nonlinear parameter γ as a function of waveguide height and waveguide width of the fundamental TE-mode at 1550 nm wavelength. The dot indicates the waveguide dimensions used in this work and the black curve indicates the zero dispersion of the waveguide.

TE-mode at 1550 nm wavelength. The high confinement of this mode translates into a small effective area A_{eff} of around $0.9 \mu\text{m}^2$ for a waveguide with dimensions of 700 nm in height and 1.65 μm in width. It is important to mention that for this cross-section dimension, both the fundamental and second order TE- and TM modes are guided for wavelengths above the L-band. For efficient nonlinear processes over a wide spectrum a low and anomalous dispersion in the waveguide structure is essential. By tailoring the dimensions of the core medium, it is possible to change the waveguide dispersion in order to overcome the normal material dispersion to obtain the desired chromatic dispersion in the waveguide. For our material combination we studied the impact of the height and width of the waveguide on the dispersion D in detail. We varied the core dimensions with steps of 30 nm for the height and in steps of 90 nm for the width and interpolated the data to achieve fine resolved dispersion information for different waveguide cross sections as presented in Fig. 3(b) for the fundamental TE-mode at 1550 nm. The plot reveals that anomalous dispersion, $D > 0$, is achieved at waveguide dimensions thicker than 600 nm. With our stress reduced Si_xN_y , those thicknesses can be manufactured without film cracking, leading to high yield and reproducibility of the processed waveguides. The dimensions of the waveguides used in this work (1.65 μm width, 700 nm height) result in anomalous dispersion of around 60 ps/(nm·km) according to the simulations.

Nonlinear processes are enhanced with higher nonlinear parameter γ that is related to the nonlinear Kerr coefficient n_2 , the wavelength λ of the optical field and the A_{eff} of the waveguide

Table 1. Comparison of nonlinear Kerr coefficient n_2 and optical band gap energy E_g for silicon, silicon-enriched nitride and stoichiometric silicon nitride.

		n_2 (at 1.5 μm) [m^2/W]	E_g [eV]
Si [24, 25]	(100% Si)	$\sim 4 \cdot 10^{-18}$	1.12
Si_xN_y	(65% Si)	$1.4 \cdot 10^{-18}$	2.3
Si_3N_4 [22, 27]	(43% Si)	$0.24 \cdot 10^{-18}$	~ 5

by

$$\gamma = \frac{2\pi n_2}{\lambda A_{\text{eff}}}. \quad (1)$$

Consequently, γ is enhanced by reducing the effective area and/or by increasing the nonlinear Kerr coefficient n_2 of the materials. We measured a nonlinear Kerr coefficient n_2 of $1.4 \cdot 10^{-18} \text{ m}^2/\text{W}$ for the silicon-enriched nitride (see section 5). The comparison of our silicon-enriched nitride composition (65% Si, 35%N) to pure silicon (100% Si) and stoichiometric silicon nitride (43% Si, 57%N) shows that the value of our material falls in between the other two as shown in Table 1 [22, 24, 25]. This is expected taking into account that the increased content of silicon comes along with an increase in nonlinearities. But one should be aware of the drawback when increasing the silicon content in a Si_xN_y compound as the optical bandgap of the material is reduced. This increases the risk of two photon absorption (TPA) and the related carrier effects when working with high optical intensities.

The ellipsometry data of the Si_xN_y material absorption serves as the basis to fit a theoretical model based on the Tauc-Lorentz dispersion relationship as described in [26]. From the model a bandgap of 2.3 eV was inferred, which is between reported values for Si and Si_3N_4 presented in Table 1 [25, 27]. To bridge an optical bandgap energy of 2.3 eV with two photons of the same wavelength, each photon needs a wavelength of 1100 nm or shorter. This provides an indirect indication that in our material, TPA should be negligible in the C-band.

Utilizing the measured n_2 for Si_xN_y and the n_2 for silica available in the literature, the nonlinear parameter γ was simulated for different waveguide dimensions as presented in Fig. 3(c), which shows results for the fundamental TE-mode at 1550 nm. From the mode solver data the A_{eff} is calculated as in [28]. As can be seen in the plot, the maximum γ is achieved at waveguide dimensions of around 0.9 μm width and 450 nm height, where the optical field confinement leads to the smallest effective area. Comparing the simulations of the dispersion with the simulations of the nonlinear parameter indicates that there is a tradeoff between achieving anomalous dispersion and the highest nonlinearities. This tradeoff is highlighted by including the line of zero dispersion in the γ simulation graph in Fig. 3(c).

5. Nonlinear experiments

Next we show the potential of our platform in integrated optics by realizing a set of experiments with CW-pumped waveguides. The setup shown in Fig. 4(a) contains two tunable CW lasers where both waves are amplified independently and controlled in polarization. In this way we ensure that no nonlinear interaction occurs in the amplifiers but only in the integrated waveguide. The amplified spontaneous emission (ASE) of the signal after the amplifier is filtered out by an optical bandpass filter (OBF), whereas the ASE of the pump is removed in the 200 GHz bandwidth common port of the wavelength-division multiplexing (WDM) coupler. After combining signal and pump in the WDM coupler both waves are launched over a tapered fiber

into the microchip containing a straight waveguide of 0.94 cm length. The polarization of both waves is optimized for maximum throughput in the nonlinear experiments. After the chip the conversion efficiency (CE), defined as $P_{\text{idler}}^{\text{out}}/P_{\text{signal}}^{\text{out}}$, is analyzed with respect to signal and pump waves at the input. We experimentally demonstrate that the FWM conversion efficiency is directly proportional to the pump power, even at high power levels where the increased silicon content may raise the concern of TPA happening. In the experiments, signal and pump waves were placed with 1 nm wavelength separation (signal 1562 nm, pump 1563 nm) to minimize the impact of dispersion in the FWM process. The signal power was kept constant at 19 dBm as the pump power was increased. At the output the idler and signal power were tracked with an optical spectrum analyzer (OSA) and the conversion efficiency is displayed in Fig. 4(b). The agreement with the numerical simulation indicates that the nonlinear measurement results follow the theoretical dependence on the pump power. The deviation from a quadratic dependence is explained by the strong signal that saturates the FWM process slightly. The numerical simulations are realized by solving the nonlinear Schrödinger equation with the split-step Fourier method. Coupling loss variations are considered in the simulations.

The group velocity dispersion was studied in a second experiment. Here, the separation of signal and pump wavelength is changed by setting the pump to 1563 nm and detuning the signal away to shorter wavelengths. Both waves were launched into the waveguide at constant power levels (signal 19 dBm, pump 30 dBm). The change in CE over signal-pump detuning is plotted in Fig. 4(c). The graph indicates a 3 dB conversion bandwidth of around 8 nm. This corresponds to a dispersion value of ~ 15 ps/(nm·km). The difference with respect to the simulation results [Fig. 3(b)] could be due to slight variations in the waveguide geometry that are within fabrication tolerance.

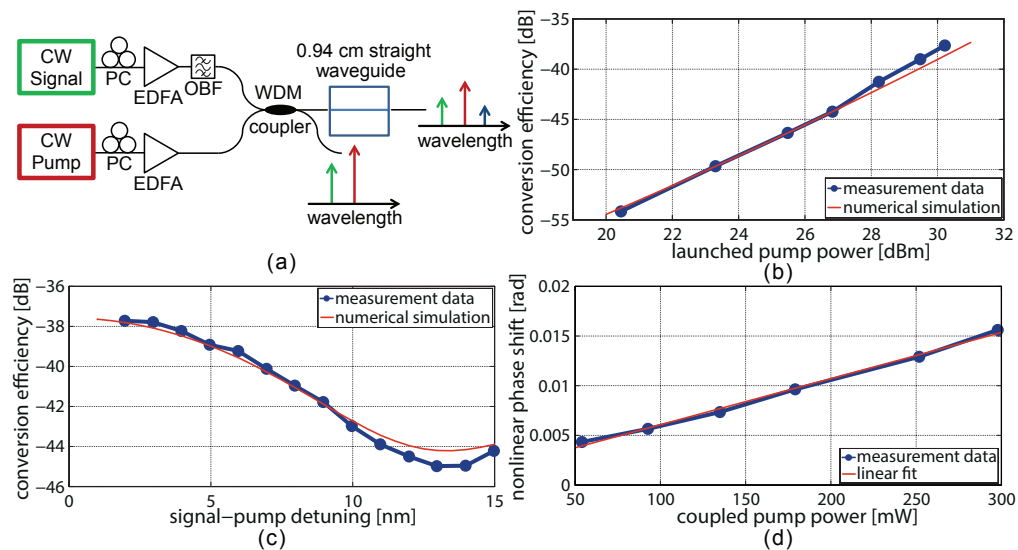


Fig. 4. (a) Schematic of experimental setup for four-wave mixing experiments. Continuous wave (CW) tunable laser. Polarization controller (PC). Erbium doped fiber amplifier (EDFA). Optical bandpass filter (OBF). Wavelength-division multiplexing (WDM) coupler. (b) Outcoupled conversion efficiency as a function of launched pump power into the waveguide. (c) Outcoupled conversion efficiency as a function of wavelength separation between signal and pump wave. (d) Nonlinear phase shift ϕ_{SPM} as a function of coupled pump power.

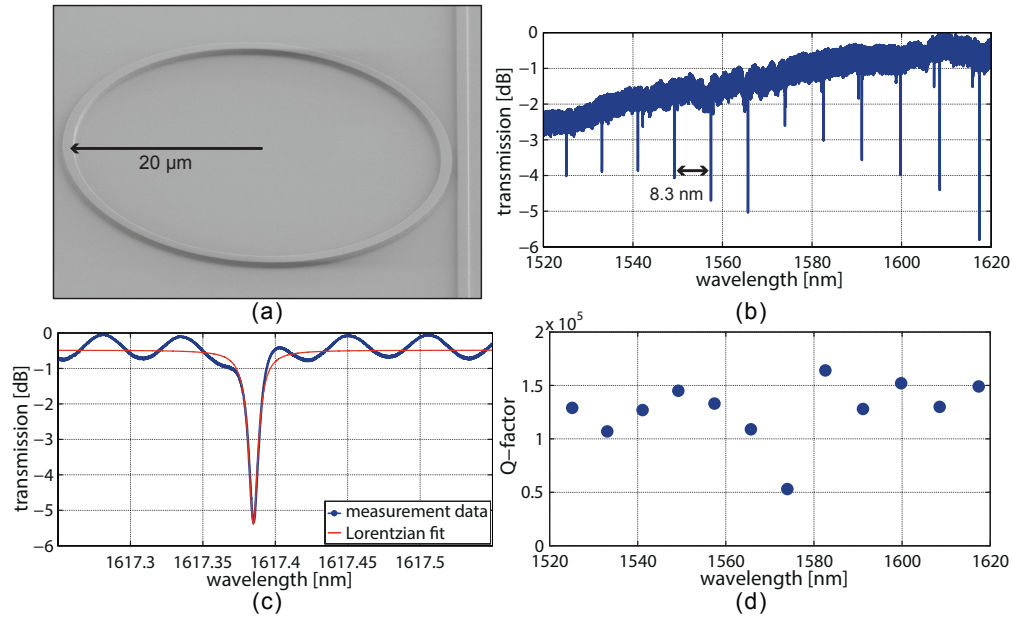


Fig. 5. (a) SEM picture of microring resonator with 20 μm bending radius at a magnification 7 000. (b) Wavelength dependent transmission spectrum of a 20 μm radius microring resonator system. (c) High-resolution scan of microring resonance at ~ 1617.4 nm. The quality factor is $\sim 150\,000$. (d) Q -factor evaluation of resonances from 1520 to 1620 nm wavelengths.

Next, we provide a characterization of the nonlinear properties in a dual CW-pumped experiment with different launched power levels, as in [29, 30]. Two CW tunable lasers are co-polarized and amplified with high-power amplifiers. The generated idler power in the waveguide with a length of 0.94 cm depends on the amount of nonlinear phase shift φ_{SPM} according to:

$$\frac{I_0}{I_1} = \frac{J_0^2(\varphi_{SPM}/2) + J_1^2(\varphi_{SPM}/2)}{J_1^2(\varphi_{SPM}/2) + J_2^2(\varphi_{SPM}/2)}, \quad (2)$$

$$\varphi_{SPM} = \gamma L_{\text{eff}} P_{\text{in}}, \quad (3)$$

Here I_0 and I_1 are the intensities of the pump wave and the idler wave of first order. J_i corresponds to the i -th order Bessel function. The ratio of nonlinear phase shift φ_{SPM} versus coupled pump power into the waveguide is $4.64 \cdot 10^{-5} (\text{mW})^{-1}$ as shown by the slope in Fig. 4(d). Following Eq. (3) and using a calculated effective length L_{eff} of 0.76 cm, a nonlinear coefficient γ of $6.1 (\text{W} \cdot \text{m})^{-1}$ is evaluated. With an effective area A_{eff} of around $0.9 \mu\text{m}^2$ the Kerr coefficient n_2 is thus $1.4 \cdot 10^{-18} \text{ m}^2/\text{W}$ using Eq. (1).

6. Compact microstructures: ring resonator

The high index contrast between the SiO_2 cladding and the silicon-enriched nitride core facilitates the fabrication of ring resonator systems with small bending radii. We manufactured a ring resonator with 20 μm bending radius as shown in the SEM picture in Fig. 5(a) taken prior to the top cladding deposition. We characterized the ring by scanning a tunable laser across a broadband window (1520-1620 nm). Optimizing the polarization for maximum throughput leads to the transmission scan shown in Fig. 5(b). The measured free spectral range of the

resonances is 8.3 nm. A zoom-in on one of the resonances measured with 0.1 pm resolution is displayed in Fig. 5(c) indicating a quality factor of around 150 000 by fitting a Lorentzian curve and evaluating the full-width half maximum in linear scale. An evaluation of the quality factor for resonances in the wavelength regime between 1520 and 1620 nm is presented in Fig. 5(d) and shows Q -factors up to 165 000. These loaded quality factors are in agreement with the measured transmission loss in Fig. 1(c).

7. Conclusion

We have presented silicon enriched nitride waveguides with a composition of 65% silicon and 35% nitrogen and discussed the advantages of having enhanced silicon content in Si_xN_y with respect to Si_3N_4 . The reduced tensile stress in the film allows thick film deposition and dispersion engineering towards anomalous dispersion, one important requirement for broadband wavelength conversion. Nonlinear characterization revealed a nonlinear Kerr coefficient n_2 of $1.4 \cdot 10^{-18} \text{ m}^2/\text{W}$ and an optical bandgap of 2.3 eV that shows the potential for high power nonlinear optics as demonstrated experimentally. High confinement in the presented waveguides and propagation loss of $\sim 1 \text{ dB/cm}$ enable high Q -factor ($\sim 1.5 \cdot 10^5$) ring resonators with small bending radii for high density of photonic integration. The waveguide loss has been evaluated to be dominated by material loss.

Acknowledgments

This work was supported by the European Research Council under grant agreement ERC-2011-AdG-291618 PSOPA, the Wallenberg Foundation and the Swedish Research Council (VR). The authors would like to thank Seyed Ehsan Hashemi for helping out with taking the AFM picture.